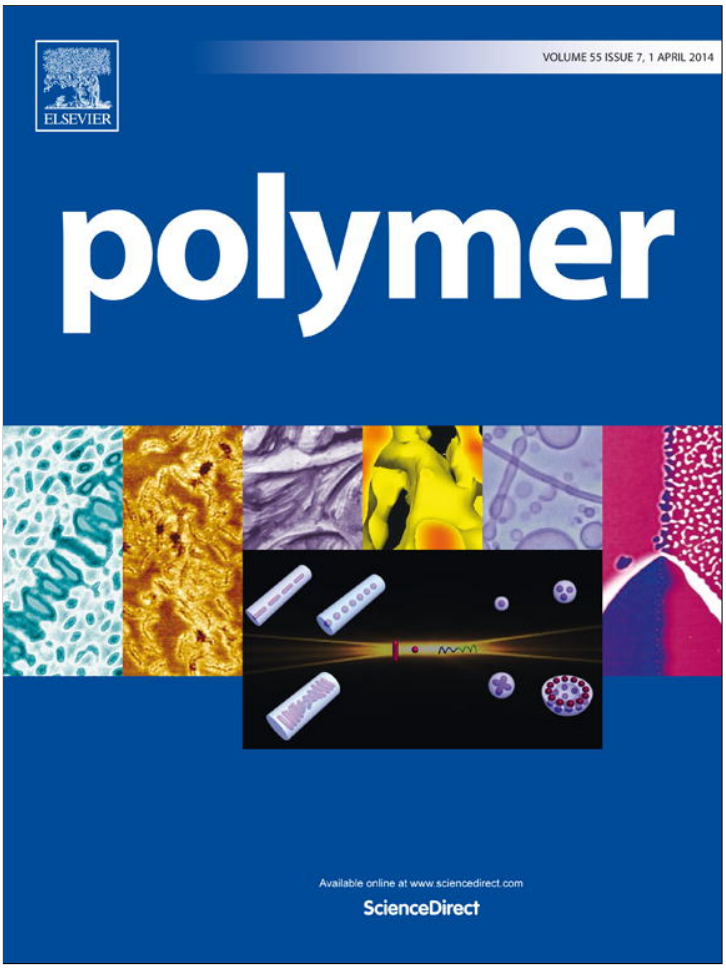

Polymer 55 (2014) 1845–1853

Contents lists available at ScienceDirect

Polymer

journal homepage: www.elsevier.com/locate/polymer

Cross-plane thermal transport in micrometer-thick spider silk films

Shen Xu [a], Zaoli Xu [a], James Starrett [b], Cheryl Hayashi [b,**], Xinwei Wang [a,*]

[a] 2010 Black Engineering Building, Department of Mechanical Engineering, Iowa State University, Ames, IA 50011, USA
[b] Department of Biology, University of California, Riverside, CA 92521, USA

ARTICLE INFO

Article history:
Received 26 November 2013
Received in revised form
30 January 2014
Accepted 5 February 2014
Available online 14 February 2014

Keywords:
Spider silk film
Raman spectroscopy
Thermal conductivity

ABSTRACT

This work reports on the first study of thermal transport capacity in the thickness direction (~μm scale) for spider silk films. Fresh (minimally processed) and hexafluoroisopropanol (HFIP) films of *Nephila clavipes* and *Latrodectus hesperus* major ampullate silk are studied. Detailed Raman spectroscopy reveals that the fresh films have more crystalline secondary protein structures such as antiparallel β-sheets than the HFIP films for *N. clavipes*. For *N. clavipes*, the randomly distributed antiparallel β-sheets in fresh films have nearly no effect in improving thermal conductivity in comparison with HFIP films. For *L. hesperus*, the films mainly consist of α-helices and random coils while the fresh film has a higher concentration of α-helices. The higher concentration of α-helices in fresh films gives rise to a higher heat capacity than HFIP films, while the thermal conductivity shows little effect from the α-helices concentration. Thickened HFIP films are heated at different temperatures to study the effect of heat treatment on structure and thermal transport capacity. These experiments demonstrate that α-helices are formed by thermal treatment and that thermal effusivity increases with the appearance of α-helices in films.

1. Introduction

For over 50 years, spider silk has attracted significant attention due to its outstanding mechanical properties. For example, with tensile strengths as high as 1.75 GPa and elongations of 26%–35% [1–3], some spider silks surpass the toughness of steel. Silk also behaves like rubber on a weight to weight basis and can be two to three times as tough as Nylon or Kevlar [4]. In addition to these superb features, with its biocompatibility and biodegradability, spider silk offers further advantages over inorganic polymers. As early as 1901, spider silk was described to be absorbable in the human body and cause low inflammation. It has also been substituted for cat-gut sutures and has become a new biomaterial for other medical applications [5,6].

Taking advantage of its excellent mechanical properties and biocompatibility, spider silk can be used in tissue engineering. Although many other artificial polymers were produced and developed a few decades ago, spider silk outperforms almost all synthetic materials [7] due to its combination of mechanical strength and elasticity [8]. Moreover, the biomedical functionality of this material could be deployed for applications in tissue replacement [9,10], suture [6,11], drug carrier [9], ligament/tendon tissue [12], biomaterial scaffold [13,14], and artificial blood vessels [5].

Compared with other kinds of fibers, the preeminent properties of spider silk come from its unique internal structure. A spider produces more than one type of silk, however, dragline silk is the most widely studied and has more desirable mechanical properties than others. Dragline silk, synthesized in the major ampullate glands in the abdomen of a spider, is composed of many parallel fibrils [15–17]. Spidroins (spider fibroins) are the main component of a silk fibril, and dragline silk in particular is composed of two spidroins, major ampullate spidroin 1 (MaSp1) and major ampullate spidroin 2 (MaSp2). In major ampullate silk, antiparallel β-sheets and random coils are the main secondary structures. The synthesis of dragline silk happens at the tail of the gland within specialized cells and then the silk proteins are stored in high concentration inside of the glands lumens as a liquid crystalline solution [18]. The liquid silk forms antiparallel β-sheets during spinning.

One approach to study the structure and properties of spider silk is to dissolve the silk protein in a solution, make a coating material to understand how the structure determines the physical properties, and then manipulate the structure [19]. Transmission electron microscopy (TEM) [20] has a higher resolution than standard optical microscopy making it very useful to observe the internal

* Corresponding author. Tel.: +1 515 294 2085; fax: +1 515 294 3261.
** Corresponding author. Tel.: +1 951 827 4322.
E-mail addresses: cheryl.hayashi@ucr.edu (C. Hayashi), xwang3@iastate.edu (X. Wang).

http://dx.doi.org/10.1016/j.polymer.2014.02.020
0032-3861/

structure of spider silk film at the nanometer-scale. Fourier transform infrared spectroscopy (FTIR) [20,21] can characterize detailed chemical bonds in spider silk proteins. Circular dichroism (CD) spectroscopy [21,22] can analyze the α-helices and the antiparallel β-sheets conformation of spider silk protein in a solvent.

In addition to the above mentioned techniques, Raman spectroscopy is a powerful method to characterize the internal structure of spider silks and it has been employed in many studies [19]. Most Raman spectra of different silk samples from various spiders show two major peaks about amide III (1220–1279 cm^{-1}) and amide I (1650–1680 cm^{-1}). These represent antiparallel β-sheets, which silks from silkworm also have. These two peaks have their own distinct locations when they are in the antiparallel β-sheets and their Raman wavenumbers shift when they are in random coils.

In spider silks, the intrinsic thermal transport capacity is strongly determined by molecular weight, structure, crystallinity and alignment. For example, defects are the main source of reduction in strength and thermal conductivity. Under the same measurement condition, better internal structures (e.g., less defect, higher crystallinity, and better alignment) will lead to higher thermal transport properties. Therefore, thermal diffusivity and conductivity can be used as signatures to reflect the protein structures of spider silks. These thermal transport properties can complement the structural information determined by other techniques (e.g., XRD, SEM, FTIR), and provide new perspectives and understanding of the structure regularity and energy coupling in spider silk, as well as other synthetic and natural polymers. Unfortunately, very little research has been done on the thermal transport capacity in spider silks, thus, there has been very little use of this property to characterize its structure variation. According to Huang's discovery, the observed exceptionally high thermal conductivity of spider silk, from 348.7 ± 33.4 to 415.9 ± 33.0 W/m·K, is largely attributed to its extraordinary well-organized and less defective structures formed from strong self-assembly [23].

This work is focused on films made from native spider silk protein (major ampullate) that have either been cast directly from freshly dissected glands or from glands dissolved in hexafluoroisopropanol, HFIP. Two spider species are studied: *Nephila clavipes* (golden orb-weaver) and *Latrodectus hesperus* (Western black widow). The structure of original samples and heat treated HFIP films are studied and correlated with the thermophysical property change, in anticipation of revealing the unique structure of spider silk films and how energy transport is achieved. Additionally, the photothermal (PT) technique is used to characterize the thermophysical properties along the thickness direction of the films of interest.

2. Sample preparations

To better understand the relationship between thermophysical properties of spider silk and protein structures from different film casting methods, two types of samples from two spider species, *N. clavipes* and *L. hesperus*, are prepared in this study. The first type of sample is major ampullate silk films that are cast on glass slides directly from freshly dissected major ampullate glands (as "fresh films" hereafter). For each slide, one pair of major ampullate glands is dissected from an individual adult female spider in 1X saline-sodium citrate (SSC) solution. The major ampullate glands are then moved to a water bath, where the surrounding gland tissue is carefully removed, leaving just the silk material. The silk material retains in the gland. The silk mass is then placed on a glass slide and flattened into a film using a spatula dipped in 50% ethanol to prevent sticking. The film is air-dried. Each *L. hesperus* fresh film contains approximately 35 μg of protein while each *N. clavipes* fresh film contains approximately 400 μg of protein. *N. clavipes* fresh films have more protein because a *N. clavipes* major ampullate gland (Fig. 2d, left) is much larger than a *L. hesperus* major ampullate gland (Fig. 2c). *N. clavipes* major ampullate glands and films are also distinguished by a bright yellow color (Fig. 2d, right and left, respectively).

The second type of films is made from major ampullate silk glands dissolved in HFIP (referred to as "HFIP films"). For *N. clavipes*, two pairs of major ampullate glands are combined in a microfuge tube. For *L. hesperus*, five pairs of major ampullate glands are combined in another microfuge tube. Each tube of glands is dissolved overnight in 1300 μL HFIP, centrifuged to remove insoluble debris, and the HFIP evaporated to about 500 μL. For each film, 100 μL of HFIP solution is spread onto a glass slide and allowed to air dry. As with the fresh films, the *Nephila* HFIP films have a bright yellow color. The *N. clavipes* and *L. hesperus* HFIP films contain approximately 140 μg and 40 μg of protein, respectively.

To make thicker HFIP films for heat treatment experiments, an 8 mm diameter washer is mounted flatwise on a glass slide. The HFIP solutions are prepared similarly as above. Specifically, for *N. clavipes*, one pair of major ampullate glands is put into a microfuge tube and for *L. hesperus*, five pairs of major ampullate glands are put in another microfuge tube. Each set of glands is dissolved in approximately 1000 μL of HFIP overnight. After centrifugation to remove insoluble debris, the HFIP is evaporated until 300 μL for *N. clavipes* and 600 μL for *L. hesperus*. These volumes are selected to approximate the same protein concentration as the previous HFIP films. For each species, 100 μL of the HFIP solution is slowly pipetted onto each glass slide in the middle of the washer

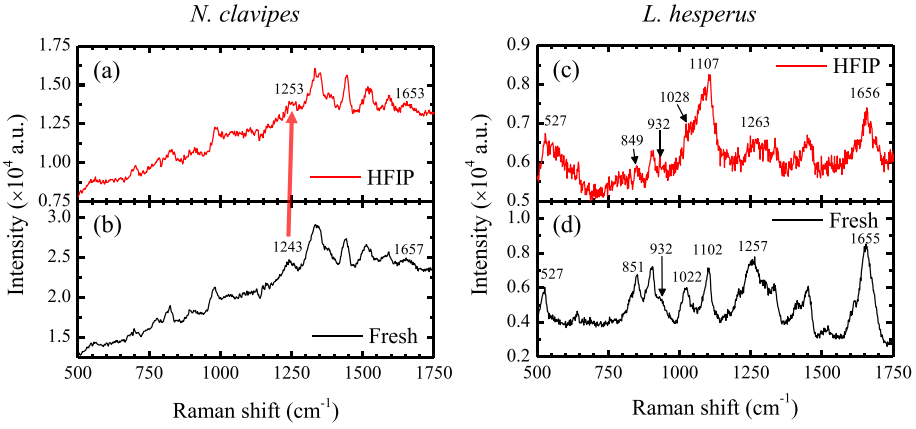

Fig. 1. Raman spectra from 500 cm^{-1} to 1750 cm^{-1} for *N. clavipes* (a) HFIP film (b) fresh film, and for *L. hesperus* (c) HFIP film and (d) fresh film. This region is tightly related to internal structures of silk films.

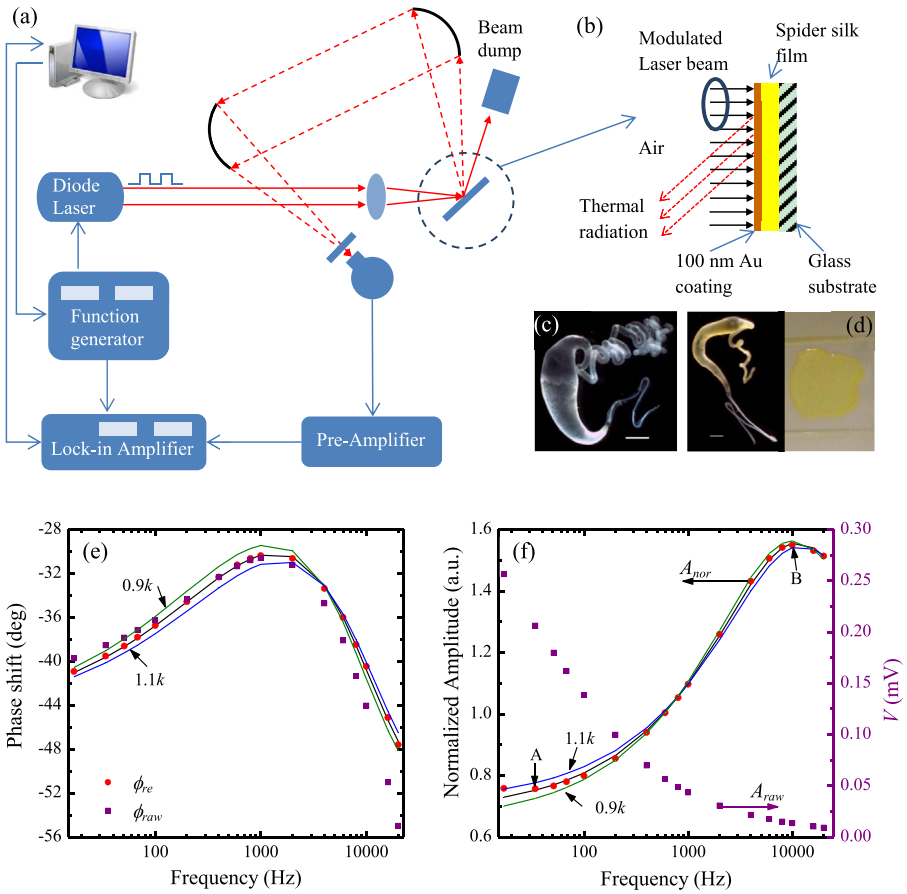

Fig. 2. (a) The setup of PT experiment. (b) The mechanism of the PT experiment showing the sample structure. (c) *L. hesperus* major ampullate gland, scale bar = 1 mm. (d) *N. clavipes* major ampullate gland (left image, scale bar = 1 mm) and HFIP film (right image). Note translucence and bright yellow color of the silk. (e) Raw phase shift ϕ_{raw} (purple squares), real phase shift ϕ_{re} after calibration (red dots), and the fitting curve (black line). The thermal conductivity is determined at 0.270 W/m·K. Theoretical curves with thermal conductivity of 0.243 W/m·K (green line) and 0.297 W/m·K (blue line) demonstrate the fitting uncertainty. The theoretical fitting agrees well with experimental data. (f) Normalized amplitude A_{nor} (red dots) and raw amplitude A_{raw} (purple squares) change with the frequency. (For interpretation of the references to color in this figure legend, the reader is referred to the web version of this article.)

and allowed to air dry. The result is a thickened HFIP film. For these thickened HFIP films, the approximate protein amounts are 135 μg and 120 μg per *N. clavipes* and *L. hesperus* films, respectively.

3. Structure characterization using Raman spectroscopy

All spider silk films are first characterized by using Raman spectroscopy and the representative spectrum of each film is shown in Fig. 1. Spectra are all recorded at room temperature (20 °C) and in open air. A confocal Raman spectrometer (Voyage, B&W Tek, Inc.) installed with a 532 nm excitation laser and a microscope (Olymoys BX51) is employed for the characterization. A 50× microscope objective is used to focus the laser beam. The beam is about 8 μm^2 at the focal spot. The glass slide is mounted on a three-dimensional nanostage (Max 311D). The resolution of the Raman spectrum is 1.05–1.99 cm^{-1}.

3.1. Films of N. clavipes

Fig. 1a and b contain two Raman spectra from 500 cm^{-1} to 1750 cm^{-1} for *N. clavipes* samples. According to previous work [24–26], most peaks in this range are related to detailed structures of the spider silk film. To get a sound spectrum, the Raman integration time is set to 10 s for the *N. clavipes* films and the laser energy is 8.6×10^8 W/m^2. *N. clavipes* silk films have a yellow color that causes a strong background as shown in the Raman spectra. Table 1 lists the important observed peaks in Fig. 1a and b, and the corresponding chemical bonds in silk proteins are assigned.

In Fig. 1a and b, profiles of both spectra are similar since they are all extracted from major ampullate glands of *N. clavipes*. The Raman intensity of the fresh film (Fig. 1b) is higher because it is thicker and has more protein than the HFIP film (Fig. 1a). The fresh liquid silk protein from major ampullate glands is viscous and quickly solidifies during sample preparation. Thus, it is hard to make the film thin. Compared with the fresh liquid silk protein, the silk protein-HFIP solution is less viscous. It covers a larger area on the glass slide and forms a thinner film. Furthermore, the fresh film contains more proteins than the HFIP film. Therefore, these two reasons likely cause the different intensities of Raman peaks for the fresh film and the HFIP film despite using the same conditions for the Raman spectroscopy. The most obvious difference between the HFIP film and the fresh film is the location of the amide III peak. The location of this peak differs in the two spectra, indicating the difference between the structures of these two samples. The broad amide III peak locates between 1243 cm^{-1} and 1253 cm^{-1} in HFIP film. It may be composed of multiple split peaks, which implies the existence of both random coils and antiparallel β-sheets. However, for the fresh film, the clear amide III peak at 1243 cm^{-1} indicates antiparallel β-sheets. They may be formed in fresh film during quick

Table 1
Detailed assignment of major peaks in Raman spectra of *N. clavipes* and *L. hesperus* major ampullate silk films [24,25].

Assignment	Peak position (cm^{-1})			
	N. clavipes		*L. hesperus*	
	Fresh	HFIP	Fresh	HFIP
Ala			527	527
			α-helices	α-helices
Fermi resonance of the Tyr doublet			851	849
α-helices			932	932
			α-helices	α-helices
In-plane stretching of benzene ring			1022	1028
Skeletal C^{α}–C^{β} stretching			1102	1107
			Random coils	α-helices and Random coils
Amide III	1243	1253	1257	1263
	β-sheets	Random coils	Random coils	Random coils
Amide I	1653	1657	1655	1656
	α-helices and Random coils	α-helices and Random coils	α-helices and Random coils	α-helices and Random coils
Mass of protein	400 μg	140 μg	35 μg	40 μg

solidification. The difference between these two films could result from the solvent used in the production of the HFIP film. The chemical $(CF_3)_2CHOH$ contains F and O elements, which can form a stronger hydrogen bond with N element in silk protein and thus will prevent protein crystals of secondary structures from forming. Therefore, it explains why fewer antiparallel β-sheets exist in HFIP film.

3.2. Films of *L. hesperus*

The same analysis is applied to Raman spectra of *L. hesperus* films. Two spectra are shown in Fig. 1c and d and detailed assignments of main peaks are also listed in Table 1. Although the HFIP film and fresh film have similar amounts of protein, as the *N. clavipes* films, the HFIP film is spread over a larger area. Therefore, the lower concentration of protein in the HFIP film compared to the fresh film is reflected by the weaker intensity of all peaks. The HFIP film has a very weak amide III peak at 1263 cm^{-1} and an amide I peak at 1656 cm^{-1}. These two locations are characteristic locations for the amide III and amide I peaks in random coils, respectively. A relatively weak and broad peak is near 527 cm^{-1}, which is assigned to alanine (Ala) configuration in α-helices. For the fresh film in Fig. 1d, it has qualitatively the same structure as the HFIP film because some locations of peaks of the fresh film match those of the HFIP film. The amide III peak of fresh film is at 1257 $cm^{-1}$and amide I peak is at 1655 cm^{-1}, and both of them represent the random coils. However, compared with the HFIP film, the fresh film has a relatively strong sharp peak at 527 cm^{-1}, indicating the existence of more α-helices. Another peak at 932 cm^{-1} refers to α-helices appearing as a shoulder in both spectra of fresh and HFIP films.

Some differences exist between these two spectra in Fig. 1c and d. The peak at 1022 cm^{-1} for the fresh film (in Fig. 1d) is clear and a little bit lower than the peak at 1102 cm^{-1}, but for the HFIP film, this peak (approximately at 1028 cm^{-1} in Fig. 1c) is weak and is overlapped by the one at 1107 cm^{-1}. This peak (1022 cm^{-1}) is assigned to the in-plane stretching of benzene ring (Phenylalanine). The fresh film has another strong peak at 851 cm^{-1}, which represents the fermi resonance of the Tyrosine (Tyr) doublet. Instead, the HFIP film shows a corresponding peak approximately at 849 cm^{-1} in Fig. 1c but its intensity is near the noise level. Both 851 cm^{-1} and 1022 cm^{-1} peaks refer to two amino side chains and can be easily detected in fresh film because the fresh film has more proteins under the focal spot. Also, more crystals in fresh film help increase the protein density. For *L. hesperus* samples, the solvent reduces the formation of protein secondary structures in HFIP films, resulting in more random coils than in fresh films.

Both *N. clavipes* and *L. hesperus* films have major peaks for random coils and α-helices mixtures. The α-helices and some other structural bonds are more clearly found in *L. hesperus* films than in *N. clavipes* films. The difference in structure between *L. hesperus* and *N. clavipes* films may be due to the proportion of MaSp1 to MaSp2. Both MaSp1 and MaSp2 have poly-alanine regions, which are expected to contribute to the α-helices. MaSp2, however, contains appreciable amounts of proline, which are less favorable for alpha helices. Based on amino acid composition data, *L. hesperus* major ampullate silk has a higher ratio of MaSp1 to MaSp2 compared to *N. clavipes* major ampullate silk (5:2 vs. 3:2, respectively) [27–30]. Raman peaks for other functional groups in random coils are more obvious for *L. hesperus* film.

4. Thermal energy transport

4.1. Fundamentals of the photothermal technique

The schematic of the Photothermal technique (PT) experimental setup is shown in Fig. 2a and its principle is shown in Fig. 2b. The original film sample is first coated with a metallic layer of a suitable thickness, and then a modulated laser is used to irradiate and heat the surface of the metallic film. The temperature of the surface rises as the surface absorbs the laser energy. Thus, when the heating laser is modulated periodically, a periodic temperature variation will occur at its surface. This temperature variation will have a phase shift relative to the modulated laser beam. This phase shift largely depends on thermophysical properties of underlayers (silk films in this work). By fitting the phase shift variation against the modulation frequency, the thermophysical properties of underlayers can be determined. Details of the PT principles and theoretical solution can be found in our previous work [31–34] and Supporting Information.

In this experiment, all silk films are first covered with a 100 nm thick Au film by using our sputter coating system (Denton: Desk V). Au is chosen for the surface coating due to its high thermal conductivity, which improves the thermal conduction between Au and samples. The optical absorption length of Au for the laser with a wavelength $\lambda = 809$ nm is 13.2 nm [35] noting that 100 nm is thick enough to protect samples from being directly excited by the laser.

The setup of the PT measurement is shown in Fig. 2a. A modulated infrared diode laser (BWTEK BWF-2) with a wavelength of 809 nm irradiates the surface of the Au layer that is on the spider silk film. The laser beam follows the Gaussian distribution and the spot size of the laser focused on the sample surface is approximately 0.7 mm × 1.4 mm [32]. It is modulated in a wide frequency

range from 17 Hz to 20,000 Hz. Its power is about 2.1 W after modulation. The thermal emission due to temperature variation on the Au surface is measured by an infrared detector (Judson Technology: J15D12). A Germanium (Ge) window is placed in front of the detector to filter the diffuse reflection and only allows the thermal emission to pass through. The signal from the infrared detector is transferred to a pre-amplifier and collected by a lock-in amplifier (Stanford Research: SR830) that is controlled by a PC for data acquisition.

In the characterization, the experimental setup will inevitably induce systematic time delay. The PT measurement is run with a clean silicon wafer with 100 nm gold coating for system time delay calibration. The Ge window is moved away and the detector collects the scattered laser light. The measured phase shift and amplitude are both used in phase shift data processing and amplitude-based data analysis as detailed below.

4.2. Thermophysical properties determination based on phase shift

After the experimental setup is calibrated, the system phase shift (ϕ_{cal}) is ruled out by directly subtracting calibration phase shift from the raw data (ϕ_{raw}) of samples. A program developed in our lab is used to fit the phase shift to determine the film properties. The results with the *L. hesperus* HFIP film (HFIP2) is shown in Fig. 2e. The purple squares represent the raw data, and the red dots are real phase shift: $\phi_{re} = \phi_{raw} - \phi_{cal}$. The black solid line is the best theoretical fitting curve for the real phase shift. The thickness of this HFIP2 film is 2.24 μm in the tested area. Using the known properties of glass substrate, gold and air [35], the calculated effective thermal conductivity k is 0.270 W/m·K and the heat capacity per unit volume $\rho \cdot c_p$ is 1.40×10^6 J/K·m^3, where ρ is density and c_p the specific heat. Fig. 2e also shows the experimental uncertainty with 10% variation in k. It is evident when the k value is changed by 10% from the best one, significant difference can be observed between the theoretical calculation and experimental data. Thus, the determined k and $\rho \cdot c_p$ have an uncertainty better than 10%.

All thicknesses d, fitted effective thermophysical properties k and $\rho \cdot c_p$, and thermal effusivity, e, of films for both *N. clavipes* and *L. hesperus* are summarized in Table 2. For *N. clavipes*, two fresh films and two HFIP films have similar k around 0.370 W/m·K. The thickened HFIP2 film (17.34 μm thick) has the largest k among four samples, which is 0.404 W/m·K. The thickened film is less smooth and uniform than other types of films. This can be explained by substances, such as protein crystals, not being well distributed during solidification. The laser spot is quite small when focused on the sample surface and that area might have higher content of substances of thermal conductivity. As revealed before in Fig. 1a and b, the fresh film has some antiparallel β-sheet crystals that the HFIP film does not have. Such structure difference gives negligible difference in thermophysical properties considering the 10% experimental uncertainty. It is hypothesized that the antiparallel β-sheet crystal in the fresh film is randomly aligned since it does not increase the thermal conductivity.

For all *L. hesperus* samples, the obtained average k and $\rho \cdot c_p$ from two fresh films are slightly larger than HFIP films. For example, they are 0.355 W/m·K and 1.78×10^6 J/K·m^3 for the fresh2 film, while for the HFIP2 film, k is about 0.270 W/m·K and $\rho \cdot c_p$ is 1.37×10^6 J/K·m^3. The difference between fresh and HFIP films should be caused by the different preparation methods. Solubilization of proteins affects the formation of internal structures when preparing HFIP films. In agreement with Raman spectra of these two kinds of samples, the HFIP film has weaker and broader Raman peaks of structures than the fresh film since the HFIP blocks the formation of hydrogen bonds in silk protein and then reduces protein crystals of secondary structures. It is well known that crystals have structures favoring thermal energy transport that random coils do not. HFIP films have more random coils than fresh films, so they have a weaker capability of transferring the heat and thus a lower k. The conclusion that the HFIP film has a lower thermal conductivity than the fresh film is not very strong since we do observe one HFIP film (HFIP1) with a higher thermal conductivity (0.435 W/m·K) than all other four films. Furthermore, due to a larger quantity of crystals, fresh films have more compact structures and thus higher $\rho \cdot c_p$ than HFIP films. Also, it is known that hydrogen bonds are good at storing thermal energy. Therefore, the low hydrogen bond concentration caused by the HFIP solution in the HFIP film will lower its heat capacitance.

Comparing the thermophysical properties of *N. clavipes* and *L. hesperus* samples, all films of *N. clavipes* have similar k, while the two types of *L. hesperus* films have different k. The k of fresh films of *L. hesperus* is similar to the *N. clavipes* samples, but the k of HFIP films of *L. hesperus* is lower, which can be attributed to their less crystalline structure. When comparing the heat capacity per unit volume: $\rho \cdot c_p$, films of *N. clavipes* have similar heat capacities. However, the *L. hesperus* films are significantly different in that the heat capacity of HFIP films is lower than fresh films because of the looser internal structures of HFIP films. Evidently, HFIP solvent has a large effect on the internal structures that form during solidification of *L. hesperus* films. This could be explained by the thin *L.* HFIP films being composed of less concentrated protein than either fresh or thickened HFIP *N.* films. With less protein, there is less opportunity for structure formation. Therefore, *L. hesperus* HFIP films have the most random coils, the smallest thermal conductivity and the lowest heat capacity.

Table 2
Thermophysical properties determination based on phase shift and amplitude.

Sample index	d (μm)	Phase shift fitting			Amplitude fitting		
		$\rho \cdot c_p$ (10^6 J/K·m^3)	k (W/m·k)	e (W·s$^{1/2}$/m^2·k)	$\rho \cdot c_p$ (10^6 J/K·m^3)	k (W/m·k)	e (W·s$^{1/2}$/m^2·k)
N. clavipes (golden orb-weaver)							
fresh1	18.58	1.57	0.365	757.0	1.53	0.547	914.8
fresh2	28.19	1.34	0.388	721.0	1.48	0.448	814.3
HFIP1	5.69	1.73	0.343	770.3	1.39	0.359	706.4
HFIP2	17.34	1.57	0.404	796.4	1.38	0.610	917.5
L. hesperus (Western black widow)							
fresh1	21.32	1.74	0.306	729.7	2.08	0.396	907.6
fresh2	6.53	1.78	0.355	794.9	1.68	0.397	816.7
HFIP1	3.39	1.14	0.435	704.2	1.20	0.668	895.3
HFIP2	2.24	1.37	0.270	608.2	1.55	0.264	639.7
HFIP3	2.06	1.31	0.280	605.6	1.67	0.270	671.5

4.3. Thermophysical properties determination based on amplitude

The amplitude of thermal radiation from the Au surface is another significant parameter we measure for calculating the thermophysical properties of samples. The k of spider silk will strongly affect the temperature rise at the Au surface during heating. If k is larger, the thermal energy in the Au layer will easily and quickly transfer into the spider silk layer so that the temperature on the Au surface will be lower than that with a lower k underlayer. We can determine the k of spider silk layer through fitting the amplitude of thermal radiation from the Au surface under different frequencies as we do in the phase shift fitting.

This amplitude fitting is a new analysis method that we developed and applied in this work. In previous studies, the amplitude data were not used to determine the film properties in the PT technique due to the fact that the amplitude is easily affected by many factors, such as the collection angle of the paraboloidal mirror, surface emissivity, and absorptivity. Fig. 2f shows the raw (A_{raw}) amplitude data of HFIP2 film of *L. hesperus* (purple square dots). The amplitude quickly decreases as the frequency increases. However, the experimental system will inevitably produce systematic uncertainty and the amplitude variation of the incident laser will also affect radiation signals. These systematic and laser effects can be eliminated by dividing the raw data of the laser amplitude (A_{cal}) measured in calibration.

Furthermore, the incident laser is modulated by a function generator during the whole PT experiment. The raw amplitude is also affected by frequency f. The measured amplitude decreases quickly as the frequency increases since the heating time is shorter in each period in the higher frequency range. The sensitivity is thus lower in the higher frequency range so that the modulation effect should be considered. The processed result A_{raw}/A_{cal} is further normalized by multiplying $\sqrt{f}$ (the physics discussed below). The final normalized amplitude, A_{nor}, is shown in Fig. 2f. Opposite to the raw data, A_{nor} is increasing with the frequency and becomes more sensitive especially in the high frequency range.

Fig. 2f also shows the fitting result (black curve) of HFIP2 film of *L. hesperus* for the normalized amplitude. The same parameters of other materials used in phase shift fitting are used in this amplitude fitting, and the fitted k and $\rho\cdot c_p$ for the spider silk film is 0.264 W/m·K and 1.55×10^6 J/K·m^3, respectively. The theoretical fitting matches the experimental results well. The uncertainty of the fitting process is also plotted as two other curves with 10% variation of k. The green curve is the curve with $k = 0.238$ W/m·K and blue curve is the curve with $k = 0.292$ W/m·K. The k from the phase shift and the amplitude fitting methods are very close to each other while there is only a slight difference between $\rho\cdot c_p$. Deviations between the two fitting methods may come from the residual calculation in the theoretical computing. Fitted results based on amplitude are summarized in Table 2 for all samples. Briefly, the amplitude fitting gives the same conclusion as the phase shift fitting about how the HFIP affects the film structure and thermophysical properties. It needs to be pointed out the amplitude fitting is based on how the normalized amplitude changes with frequency, and does not use absolute values. It has less accuracy when compared with the phase shift fitting. Nevertheless, it provides a reasonable comparison to check the phase shift fitting results.

When the laser irradiates the Au surface of the sample, the energy input amount depends on the irradiation time and incident intensity. The total incident energy, ΔE, arriving at the sample surface in one heating period is $\Delta E = 0.5\varepsilon I_0/f$, where I_0 is the laser intensity, and ε the surface absorptivity. ΔE is proportional to A_{cal} (scattering signal) measured in calibration. The longer the laser radiates, the higher the temperature rise. The thermal diffusion length $L = \sqrt{\alpha/f}$ depends on both thermal diffusivity α and frequency f, so a higher frequency will shorten the diffusion length and concentrate the absorbed energy into a smaller depth. Amplitude A_{raw} from the lock-in amplifier is the combination of these two factors,

$$A_{raw} \sim \frac{\zeta \Delta E}{\sqrt{\alpha/f}\cdot\rho\cdot c_p}, \tag{1}$$

where ζ is a coefficient related to other factors in the experiment, including detector sensitivity, surface emissivity, and collection angle. ζ is a constant across all the frequencies. The normalized amplitude A_{nor}, can be expressed by

$$A_{nor} = \frac{\zeta A_{raw}\cdot\sqrt{f}}{A_{cal}} \sim \frac{\zeta}{\sqrt{k\cdot\rho\cdot c_p}} \tag{2}$$

It shows that the normalized amplitude is related to effusivity of the sample: $e = \sqrt{k\cdot\rho\cdot c_p}$, including that of the spider silk film and glass substrate.

Data points A ($f_A = 51$ Hz) and B ($f_B = 10{,}000$ Hz) in Fig. 2f are selected for further discussion of the amplitude fitting method. Point A is in the low frequency region and B is in the high frequency region. Based on the data shown in Fig. 2f, we have $A_{nor,B}/A_{nor,A} = 2.07$. The amplitude value at point B is largely determined by the properties of spider silk since the thermal diffusion length is very short, mostly constrained within the film thickness. In the low frequency range, heat transfer has a long diffusion depth, passing the film, and significantly penetrating into the glass substrate. So $k\cdot\rho\cdot c_p$ is mostly the property of pure glass slide. To test our results, the values of density, specific heat and thermal conductivity of glass from Ref. [35] and spider silk we measured based on phase shift are used here. The ratio of $k\cdot\rho\cdot c_p$ of glass to that of the spider silk is 5.6. Thus, based on Eq. (2), we have $A_{nor,B}/A_{nor,A} \sim \sqrt{(k\rho c_p)_{spider}/(k\rho c_p)_{glass}} = 2.37$, which is very close to the ratio directly calculated from the normalized amplitude: 2.07. This estimation is slightly larger than the experimental figure because $k\cdot\rho\cdot c_p$ is not the exact value of the pure glass in the low frequency range. Both spider silk and glass will affect the amplitude of thermal radiation from the Au surface. In the high frequency range, glass has a very weak effect on the surface radiation since the thermal diffusion length is quite short in the spider silk layer.

4.4. Thermal treatment

Heat treatment can provide an opportunity to transform the internal structure of spider silk proteins. Previous works showed that random coils will transform into secondary structures by using heating process, such as α-helices and antiparallel β-sheets [36]. In this work, heat treatment is applied to the thickened HFIP films to study the transformation of protein structures. Films are heated at 20 °C, 40 °C, 60 °C, 80 °C, 95 °C, 120 °C, 140 °C, 160 °C, and 180 °C, respectively, with one temperature per run. For temperatures below 100 °C, films are placed in a glass jar sealed with a cap in a water bath. The temperature of the water around the glass container is maintained for 4 h. For temperature over 100 °C, the sample is directly heated in an oven. A thermal couple is placed next to the sample to verify that the heating temperature achieved in the oven matches the instrument setting. Both *N. clavipes* and *L. hesperus* thickened HFIP films are heated at every temperature. All films burned at 200 °C. Since the PT experiments are done at room temperature, for consistency between PT and Raman measurements, Raman spectra are collected after each sample is cooled down at ambient room temperature for about 1 h, and then the PT technique is applied to study the sample's thermophysical properties.

For the *N. clavipes* thickened HFIP film, Fig. 3a and b shows variations of Raman spectra and effusivity with increasing heat treatment temperatures. Comparing the spectrum in Fig. 1a and the one of 20 °C in Fig. 3a, we find that the former has more peaks. The only difference in producing these two kinds of films is the solidification process; the protein stock and solvents are the same. It may be caused by the different surface extension. For the HFIP film used in the previous section, the spider silk solution is dropped on a glass slide to form a film without restriction, and the surface extension is the only factor affecting the film shape. However, for the thickened HFIP film, the solution is pipetted slowly in a fixed washer and the shape of the film is maintained during drying. The effect of surface extension should be smaller.

The Raman spectra remain the same for this film at 20 °C and 40 °C as shown in Fig. 3a. The crystallization starts at 60 °C demonstrated by the shift of peaks. The 1086 cm^{-1} peak at 20 and 40 °C shifts to 1101 cm^{-1} at 60 °C. This means the C—C skeletal bond configuration changes from unordered status to α-helices [37]. It could be caused by the high thermal energy and the evaporation of residual HFIP in the film. Heat energy enhances the movement of molecules and more hydrogen bonds form between polar groups in proteins and favor crystal formation. Furthermore, the boiling point of HFIP is 58.2 °C. Since all film samples are air dried, there should be a small amount of HFIP in them. When the heating temperature reaches 60 °C, the hydrogen bond between HFIP and protein breaks and the HFIP molecules dissipate into the air. The left polar groups can then connect with others and thus increase the hydrogen bonding within and among protein molecules. Moreover, the 1641 cm^{-1} peak at 20 °C and 40 °C shifts to 1662 cm^{-1} after heat treatment at 60 °C. This is also caused by the formation of α-helices [38]. As the temperature continues to increase, peaks become weaker in the Raman spectrum and the background of the spectrum increases. This background of the spectrum is caused by the yellow color of the film itself and the carbonization of protein at high temperatures since films are heated in the open air. During heating, the high thermal energy and the interaction between proteins and gas molecule may cause the unstableness and the break of the hydrogen bonds.

Fig. 3b shows the measured effect of heat treatment on effusivity. One film is continuously used in all heating runs and the thickness of this film is considered to be constant throughout the experiment. The thickness is about 11.43 μm for the *N. clavipes* thickened HFIP film. The thermal effusivity is used to explain the thermophysical properties of the film in the PT experiment because the error induced by thickness can be ruled out during the fitting process. Below 60 °C, the effusivity is about 800 $W \cdot s^{1/2}/m^2 \cdot K$, and it starts increasing at 60 °C, the beginning of crystalline formation. A sharp decrease appears in the effusivity curve at 140 °C. This temperature is close to the burning point, and silk proteins begin degrading due to the dehydration and oxidation at such high temperature. Random coils fragment into small pieces. The carbonization of proteins also starts at this temperature, with the film darkening due to some proteins becoming carbon. After the temperature exceeds 140 °C, the thermal effusivity and conductivity increase largely because of the increase of carbon content. At 200 °C, the film is completely dark and burned in appearance. $\rho \cdot c_p$ is expected to be constant since the heating process does not change the profile of the film before it is burned, so the thermal conductivity should increase just like the effusivity.

Compared to the equivalent sample from *N. clavipes*, the *L. hesperus* thickened HFIP film shows poor adhesion to the glass substrate. It easily peels off after heating at 95 °C so only four Raman spectra and effusivity are recorded for this film. The film thickness is 10.43 μm for the *L. hesperus* thickened HFIP film (film 1). Before heating the film, the Raman spectrum only has two observed peaks at 550 cm^{-1} and 1089 cm^{-1}, as shown in Fig. 4a. This characterization is different from the thin *L. hesperus* HFIP film described in the previous section. The thin HFIP film contains some α-helices while the thickened HFIP films mainly contain random coils before heat treatment. Although the thickened HFIP films have a higher amount of protein (120 μg), few crystals form in this film. However, the Raman spectrum of the thickened HFIP film is similar to that for *N. clavipes* at 20 °C. This similarity indicates that both films contain mostly random coils in films and no protein crystal is observed. In Fig. 4a, no change happens in the Raman spectrum after heat treatment at 40 °C. However, for the spectrum after 60 °C treatment, new peaks suddenly appear in the spectrum. Peaks at 528 cm^{-1}, 1101 cm^{-1} and 1657 cm^{-1} represent the existence of α-helices in the film. Those peaks begin to disappear when the heating temperature continuously increases beyond 60 °C. This can be explained by the heat treatment enhancing the movement of molecules and the breaking of hydrogen bonds.

In Fig. 4b, the effusivity of the HFIP film remains nearly constant before 60 °C and starts increasing largely after that. For the effusivity increase from 60 to 80 °C, although the crystallinity structure disappears, the temperature increase in heating will induce H-bond breaking among molecular chains. This will reduce the phonon scattering among molecular chains, and lead to an increased phonon mean free path. Therefore, the thermal transport capacity will increase, and the thermal effusivity will increase as well. This

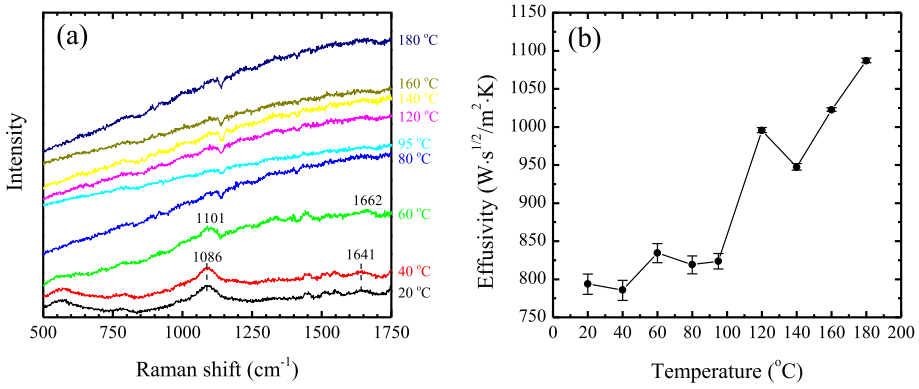

Fig. 3. (a) Raman spectra of the thickened major ampullate HFIP silk film of *N. clavipes* heated under different temperatures. The observed crystallization happens at 60 °C as peaks shift to the wavenumber representing α-helices in the Raman spectrum. These Raman peaks weaken and disappear gradually under continued heating processes. (b) The effusivity with error bars of this film after heat treatment at different temperatures.

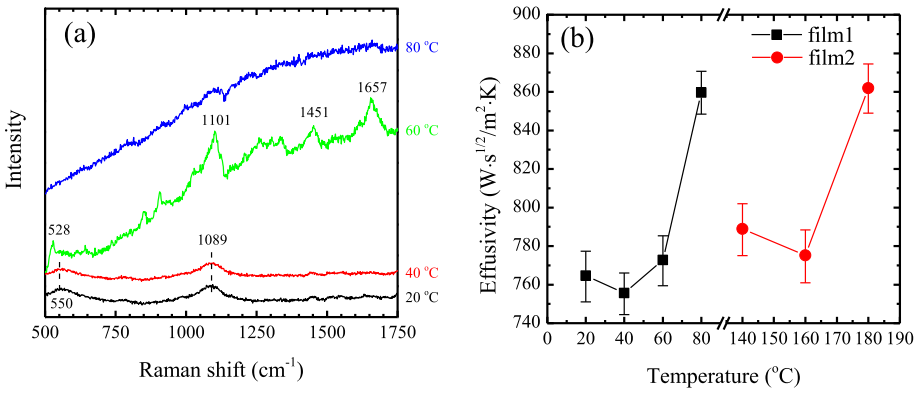

Fig. 4. (a) Raman spectra of the thickened major ampullate HFIP silk film of *L. hesperus* heated under different temperatures. The observed crystallization happens at 60 °C as some clear and representative peaks appear in the Raman spectrum. This crystal structure disappears after being heated at 80 °C. (b) The effusivity with error bars of this film after heat treatment at different temperatures.

also explains the effusivity increase from 100 to 120 °C for *N. clavipes* films shown in Fig. 3b. Another *L. hesperus* thickened HFIP film (film 2) is heated from 140 °C. It also shows an obvious decrease before burning at 160 °C, as with the *N. clavipes* film. Random coils in these thickened HFIP films of spiders will transform into α-helices and no β-sheet is observed during heat treatment. The formation of α-helices will increase the thermal effusivity and conductivity as the heating temperature increases, but a sharp decrease is observed for these two types of films before they are burned.

5. Conclusions

This study focused on the thermal transport capacity in the thickness direction for fresh films and HFIP films cast with major ampullate liquid silk protein of two spiders, *N. clavipes* and *L. hesperus*. Confocal Raman spectroscopy was conducted to characterize the structures of these samples, and the thermal properties were measured by using the PT technique. The fresh films had more crystalline secondary protein structures such as antiparallel β-sheets than the HFIP films for *N. clavipes*, but both films had similar thermal conductivities. A few randomly distributed antiparallel β-sheets in the fresh film had nearly no effect on the thermal conductivity. For *L. hesperus*, the films primarily consisted of α-helices and random coils. Since the fresh film had a higher concentration of α-helices than the HFIP film, its thermal conductivity and thermal capacity were larger than those of HFIP films. However, the effect of α-helices on thermal conductivity increase is rather weak in comparison with its effect on heat capacity. Moreover, the thickened HFIP films were heated at different temperatures to study the effect of the heat treatment on the internal structure of spider silk films. α-helices were formed during the heating process and the thermal effusivity increased when α-helices appeared in the spectra for films of both kinds of spiders. Since the internal structures largely affect thermal conductivities of spider silk films, measuring thermal properties provides an alternative way to looking at the crystalline structures of spider silk proteins, their structure regularity, and energy coupling.

Acknowledgment

Support of this work by the Army Research Office (W911NF-12-1-0272) and Office of Naval Research (N000141210603) is gratefully acknowledged.

Appendix A. Supplementary data

Supplementary data related to this article can be found online at http://dx.doi.org/10.1016/j.polymer.2014.02.020.

References

[1] Ko FK, Kawabata S, Inoue M, Niwa M, Fossey S, Song JW. Mater Res Soc Symp Proc 2001;702. U1.4.1.
[2] Zemlin JC. A study of the mechanical behavior of spider silks. Waltham, Massachusetts: Collaborative Research, Inc.; 1968. pp. 68.
[3] Denny M. J Exp Biol 1976;65:483–506.
[4] Romer L, Scheibel T. Prion 2008;2(4):154–61.
[5] Altman GH, Diaz F, Jakuba C, Calabro T, Horan RL, Chen J, et al. Biomaterials 2003;24(3):401–16.
[6] Leal-Egaña A, Scheibel T. Biotechnol Appl Biochem 2010;55(3):155–67.
[7] Yang Y, Chen X, Shao ZZ, Zhou P, Porter D, Knight DP, et al. Adv Mater 2005;17(1):84–8.
[8] Cunniff PM, Fossey SA, Auerbach MA, Song JW, Kaplan DL, Adams WW, et al. Polym Adv Technol 1994;5(8):401–10.
[9] Pritchard EM, Wilz A, Tianfu L, Jing-Quan L, Boison D, Kaplan DL. Sustained-release silk biomaterials for drug delivery and tissue engineering scaffolds. In: Bioengineering conference, 2009 IEEE 35th annual northeast; 2009. pp. 1–2.
[10] MacIntosh AC, Kearns VR, Crawford A, Hatton PV. J Tissue Eng Regen Med 2008;2(2–3):71–80.
[11] Cao Y, Wang B. Int J Mol Sci 2009;10(4):1514–24.
[12] Wang C-CR. Chlorophyll and silk-based oxygen producing biomaterials for tissue engineering. Department of Biomedical Engineering, Ph.D. Medford, MA: Tufts University; 2010.
[13] Ubaldo A, Ilaria DP, Anna C, Gi F. Int J Burn Trauma 2011;1(1):27–33.
[14] Kim HJ, Kim U-J, Kim HS, Li C, Wada M, Leisk GG, et al. Bone 2008;42(6):1226–34.
[15] Mergenthaler DB, Pietralla M, Roy S, Kilian HG. Macromolecules 1992;25(13):3500–2.
[16] Choy CL, Wong YW, Yang GW, Kanamoto T. J Polym Sci Part B Polym Phys 1999;37(23):3359–67.
[17] Shen S, Henry A, Tong J, Zheng RT, Chen G. Nat Nanotechnol 2010;5(4):251–5.
[18] Xu M, Lewis RV. Proc Natl Acad Sci U S A 1990;87(18):7120–4.
[19] Shao ZZ, Vollrath F, Yang Y, Thogersen HC. Macromolecules 2003;36(4):1157–61.
[20] Renault A, Rioux-Dube JF, Lefevre T, Beaufils S, Vie V, Paquet-Mercier F, et al. Langmuir 2013;29(25):7931–8.
[21] Spiess K, Wohlrab S, Scheibel T. Soft Matter 2010;6(17):4168–74.
[22] Huemmerich D, Slotta U, Scheibel T. Appl Phys A Mater Sci Process 2006;82(2):219–22.
[23] Huang XP, Liu GQ, Wang XW. Adv Mater 2012;24(11):1482–6.
[24] Lefevre T, Paquet-Mercier F, Rioux-Dube JF, Pezolet M. Biopolymers 2012;97(6):322–36.
[25] Rousseau ME, Lefevre T, Beaulieu L, Asakura T, Pezolet M. Biomacromolecules 2004;5(6):2247–57.
[26] Vierra C, Hsia Y, Gnesa E, Tang S, Jeffery F. Spider silk composites and applications. In: Cuppoletti J, editor. Metal, ceramic and polymeric composites for various uses. InTech; 2011.
[27] Casem ML, Turner D, Houchin K. Int J Biol Macromol 1999;24(2–3):103–8.
[28] Hinman MB, Lewis RV. J Biol Chem 1992;267(27):19320–4.
[29] Sponner A, Schlott B, Vollrath F, Unger E, Grosse F, Weisshart K. Biochemistry 2005;44(12):4727–36.
[30] Ayoub NA, Hayashi CY. Mol Biol Evol 2008;25(2):277–86.

[31] Hu HP, Wang XW, Xu XF. J Appl Phys 1999;86(7):3953–8.
[32] Wang XW, Zhong ZR, Xu J. J Appl Phys 2005;97(6):064302.
[33] Wang T, Wang XW, Zhang YW, Liu LY, Xu L, Liu Y, et al. J Appl Phys 2008;104(1):013528.
[34] Chen XW, He YP, Zhao YP, Wang XW. Nanotechnology 2010;21(5):055707.
[35] Lide DR. CRC handbook of chemistry and physics. Boca Raton, FL: Taylor and Francis; 2007.
[36] Magoshi J. Kobunshi Ronbunshu 1974;31(7):463–5.
[37] Shao Z, Vollrath F, Sirichaisit J, Young RJ. Polymer 1999;40(10):2493–500.
[38] Lefevre T, Rousseau ME, Pezolet M. Biophys J 2007;92(8):2885–95.